

Article

Au Nanoparticle-Loaded UiO-66 Metal–Organic Framework for Efficient Photocatalytic N₂ Fixation

Zehui Zhao , Guangmin Ren, Xiangchao Meng  and Zizhen Li * 

Key Laboratory of Marine Chemistry Theory and Technology, Ministry of Education, College of Chemistry and Chemical Engineering, Ocean University of China, Qingdao 266100, China; zhaozehui@stu.ouc.edu.cn (Z.Z.); 17568022691@163.com (G.R.); mengxiangchao@ouc.edu.cn (X.M.)

* Correspondence: lizizhen@ouc.edu.cn

Abstract: In order to achieve efficient photocatalytic N₂ reduction activity for ammonia synthesis, a photochemical strategy was used in this work. UiO-66 was prepared through the solvothermal method and further loaded with Au nanoparticles (Au NPs) onto the UiO-66 (Zr) framework. The experimental results verified that there were metal–support interactions between Au NPs and UiO-66; this could facilitate charge transfer among Au NPs and UiO-66, which was beneficial to enhance the photocatalytic activity. The best N₂ fixation effect of Au/UiO-66 with a loading of 1.5 wt% was tested, with a photocatalytic yield of ammonia of 66.28 μmol g⁻¹ h⁻¹ while maintaining good stability. The present work provides a novel approach to enhancing photocatalytic N₂ fixation activity by loading NPs onto UiO-66.

Keywords: photocatalytic; N₂ fixation; UiO-66; Au nanoparticles

1. Introduction

Ammonia is one of the most important industrial chemicals and has been recently considered an ideal carrier for hydrogen storage [1–3]. The reduction of N₂ to NH₃ is very hard under environmental conditions because of the intrinsic nature of the N≡N bonding, and nitrogen fixation itself is a multistep process that is kinetically complex and thermodynamically challenging [4–6]. In recent years, more than 90% of NH₃ production has been mainly dependent on Haber–Bosch technology that operates at critical conditions (i.e., 15–25 MPa and 673–873 K), which involves the catalytic synthesis of ammonia from nitrogen and hydrogen over an iron-based catalyst. However, it consumes enormous quantities of fossil resources and releases huge amounts of CO₂ [7–9]. Therefore, it is important to develop a green synthesis pathway for reducing N₂ to NH₃ under mild conditions. The photocatalytic nitrogen reduction reaction (NRR) initiated by renewable solar energy has a very promising future as an environmentally friendly, low-cost, and sustainable route for NH₃ synthesis, which converts N₂ to NH₃ ($2\text{N}_2 + 6\text{H}_2\text{O} = 4\text{NH}_3 + 3\text{O}_2$) using abundant solar energy and water at ambient temperature and pressure, avoiding the need for H₂ and harsh reaction conditions [10–12]. However, the high recombination of photogenerated charge carriers and the sluggish reaction kinetics have resulted in low photocatalytic activity in the production of ammonia [13–15]. Therefore, it is essential to rationally design the photocatalysts for a highly efficient conversion of N₂ into ammonia [16].

Metal–organic frameworks (MOFs) have been widely applied in catalysis, adsorption, separation, and sensors because of their low cost, good stability, and large specific surface area [13,17–19]. Compared to other MOFs, UiO-66 based on Zr-oxo clusters exhibits relatively high thermal and chemical stability, a highly tunable defect structure, large specific surface areas, and a stable framework [17,20,21]. Therefore, UiO-66 is widely used in photocatalysis for nitrogen fixation [22], CO₂ reduction [23], and H₂ production [24]. Importantly, functional units can be anchored in the nodes, linkers, or cavities of these Zr-MOFs. First, different kinds of active species can be immobilized in the cavities of



Citation: Zhao, Z.; Ren, G.; Meng, X.; Li, Z. Au Nanoparticle-Loaded UiO-66 Metal–Organic Framework for Efficient Photocatalytic N₂ Fixation. *Processes* **2024**, *12*, 64. <https://doi.org/10.3390/pr12010064>

Academic Editor: Chiing-Chang Chen

Received: 7 December 2023

Revised: 23 December 2023

Accepted: 25 December 2023

Published: 27 December 2023



Copyright: © 2023 by the authors. Licensee MDPI, Basel, Switzerland. This article is an open access article distributed under the terms and conditions of the Creative Commons Attribution (CC BY) license (<https://creativecommons.org/licenses/by/4.0/>).

MOFs, which impart the resulting MOF composites with better performances than the MOF itself due to the synergistic effect of the different components [25,26]. Second, a range of catalyst supporters, such as porphyrin and bipyridine, can be incorporated into the linkers, thus endowing MOFs with excellent physiochemical properties [27,28]. Thus, rational tailoring and engineering of MOFs may be exploited to markedly advance the photocatalytic fixation of nitrogen [29,30]. Unfortunately, MOFs suffer from drawbacks like limited selectivity and reproducibility [31,32]. Hence, they have to be modified using post-synthesis strategies. The modification of UiO-66 materials with loaded metals has been reported as an effective method to enhance their photocatalytic nitrogen fixation activity. These metal species can modulate the partial electronic structure surrounding defects, promote N₂ excitation, and inhibit charge complexation [33–35]. In recent years, many nanoparticle-scale (NP) catalysts have been successfully prepared using MOFs as carriers, exhibiting high photocatalytic properties [36–39]. For the photocatalytic nitrogen fixation reaction (NRR), MOF-based NPs have the following advantages: (i) MOF carriers have high N₂ adsorption ability to enrich the N₂ concentration around the active NP sites; and (ii) the metal–carrier interactions between the NPs and the MOFs significantly accelerate the charge transfer, which enhances the catalytic properties by providing a suitable electronic environment [32,36,40,41]. Among them, gold (Au) is considered an excellent catalyst for ammonia synthesis [42–44]. As is known, sulfur and nitrogen groups have particular affinity for Au(III), as the ligand is able to develop stabilizing complexes with Au(III) by chelating or complexing [36,45]. Therefore, Au(III) was selectively grown on the shell layer of UiO-66 to enhance UiO-66's activity. Presently, NPs derived from MOFs are mostly prepared through the thermal excitation method, which mostly involves complex synthesis processes, expensive equipment, or cumbersome post-processing. Even more seriously, the MOF structure may be destroyed, leading to a decrease in their gas absorption capacity and chemical stability [46,47]. Hence, it is urgent to develop efficient photocatalysts by loading metals onto MOFs through a simple room-temperature photochemical method. By constructing active sites onto MOFs through the room-temperature photochemistry method, the photogenerated electrons can be moved to the surface of UiO-66, leading to metal nanoparticle loading, thus providing sufficient N₂ adsorption sites and electron transfer channels and thus enhancing photocatalytic N₂ fixation activity.

Herein, UiO-66 in octahedral morphology was first fabricated using the solvothermal method and further loaded with Au nanoparticles (Au NPs) onto UiO-66 (Zr) frameworks using a room-temperature photochemical strategy. The experimental results showed that Au/UiO-66 exhibited more efficient photocatalytic performance in the reduction of N₂ to NH₃ than UiO-66, which was probably due to the active Au sites loaded onto UiO-66 as well as the efficient separation of photogenerated electron–hole pairs. Combined with experimental results and spectral analysis, the mechanism of the separation and transfer action of the photogenerated carriers was elucidated. In general, this work provides novel insights for the construction of surface catalytic sites at the nanoscale to optimize the reaction pathways in the multielectron N₂ photoreduction process and enhance the activity of photocatalytic ammonia synthesis reactions.

2. Materials and Methods

2.1. Materials

All chemicals, including gold (III) chloride (AuCl₃, AR), zirconium tetrachloride (ZrCl₄, 99%), and terephthalic acid (H₂BDC, 99%), were purchased from Aladdin Ltd. (Shanghai, China). N,N-dimethylformamide (DMF, 99.9%) was obtained from Macklin Ltd. (Shanghai, China), and methanol (CH₃OH) was bought from Sinopharm Chemical Reagent (Shanghai, China). All chemicals were used directly, without further treatment. The ultrapure water used in the experiments was purified using a Millipore system (Chengdu, Sichuan, China).

2.2. Materials Synthesis

Synthesis of UiO-66 catalysts: Firstly, 169 mg of $ZrCl_4$ and 121 mg of H_2BDC were dissolved in a mixed solution of 28 mL DMF in a 50 mL Teflon-capped jar (Anhui Kemi Instrument Co., Ltd, Hefei, China). The mixture was blocked and reacted at 120 °C for 12 h. The product was gathered by centrifugation and washed three times using DMF and methanol, then sequentially immersed in methanol, and the solvent was changed every 12 h for 36 h. Finally, UiO-66 was dried by removing the solvent in a vacuum dryer overnight.

Synthesis of Au/UiO-66 catalysts: A total of 0.50 g of UiO-66 was first dissolved in 100 mL of a 10% methanol–water solution and then sonicated for 30 min. A $AuCl_3$ solution was added to the UiO-66 dispersion while stirring. The suspensions were continually bubbled with high-purity N_2 (>99.99%) for 30 min while stirring in the dark prior to illumination. The dispersion was then treated with UV light as described above, with stirring at room temperature. After 60 min of illumination, the light gray Au/UiO-66 product was gathered by centrifugation and further washed with water. After being dried in a vacuum oven, the product was used for a variety of characterizations and analytical tests. The loading content of Au could be easily adjusted by introducing different amounts of $AuCl_3$ solution. The fabrication of Au/UiO-66 is shown in Figure 1.

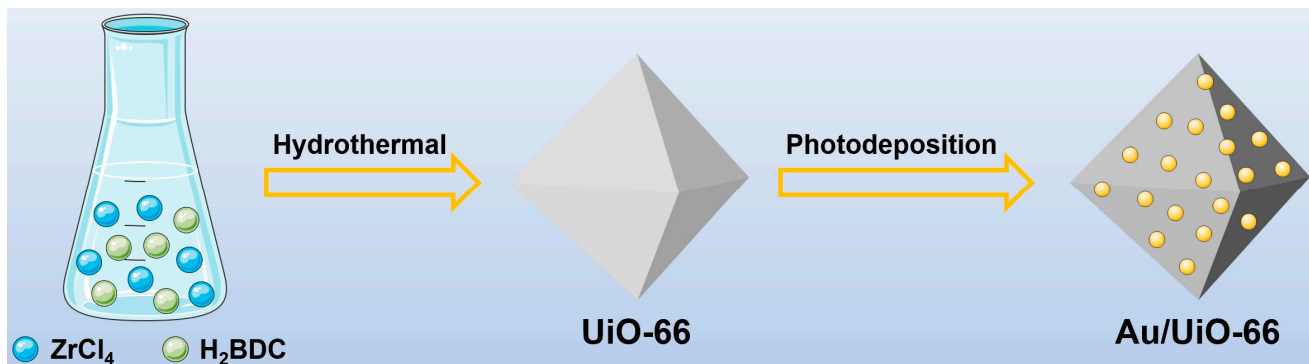


Figure 1. Schematic illustration of the preparation of Au/UiO-66.

Synthesis of M/UiO-66 (M = Pt, Pd, Ag, Ru) catalysts: Similarly, M/UiO-66 catalysts (M = Pt, Pd, Ag, Ru) were also synthesized by a procedure similar to that described above for the preparation of Au/UiO-66, utilizing H_2PtCl_6 , $PdCl_2$, $AgNO_3$, and $RuCl_3$ as precursors, respectively.

Thereafter, unless otherwise noted, the following discussion will mainly focus on UiO-66 at a Au loading of 1.5 wt% (denoted as Au/UiO-66), which exhibited the best photocatalytic nitrogen fixation activity.

2.3. Characterizations

The X-ray diffraction (XRD) patterns taken by Rigaku RINT 2500 TTRAX-III (Rigaku Corporation, Tokyo, Japan) with $Cu K\alpha$ radiation were used to characterize the phase composition and phase type of the prepared samples. The structural and morphological features of the samples were studied by scanning electron microscopy (SEM, ZIESS Gemini 300, Oberkochen, Germany) with EDX spectroscopy spectra attached. The detailed structure and surface topography of the sample were investigated by transmission electron microscopy (TEM, HT 7700, Tokyo, Japan) and high-resolution transmission electron microscopy (HRTEM, FEI Tecnai G2 F30, FEI, Hillsboro, OR, USA) operated at 300 kV. The valence state and elemental composition of the prepared compounds were determined by X-ray photoelectron spectroscopy (XPS, Thermo Scientific K-Alpha, Thermo Fisher Scientific, Cambridge, UK) with monochromatized $Al-K\alpha$ ($h\nu = 1486.60$ eV). The UV-Vis Diffused Reflectance Spectra (DRS) of the samples were recorded using a TU-1901 spectrophotometer (Pu xi Ltd. of Beijing, China). The prepared material was detected in the range of 200–800 nm to detect the band gap of the catalyst. Photoluminescence (PL) was

recorded using an F-7000 fluorescence spectrophotometer (Hitachi, Tokyo, Japan) to study the recombination and migration of electron–hole pairs under 320 nm excitation.

2.4. Photocatalytic N₂ Fixation Tests

For the ammonia production test of the photocatalytic nitrogen fixation experiment, 30 mg of photocatalysts and 60 mL of distilled water were first added to the photoreactor. After fully sealing the reactor, N₂ (>99.999% purity) was bubbled in a sealed reactor for 30 min to remove any possible nitrogen contaminants. Afterwards, the reactor was continuously irradiated for 1 h at full spectrum using a 300 W Xe lamp (Beijing Perfect Lighting Co., Ltd., Beijing, China). The distance from the lamp to the vessel was calculated to be approximately 11 cm, and the average light intensity was 491 mW cm⁻² (measured by an optical power meter (CEL-NP2000-2(10)A, Beijing, China)). After the reaction, 10 mL of solution was withdrawn and filtered through a 0.22 μm filter membrane in order to remove the residual catalyst. It was then injected into a 10 mL small glass vial to which Nessler was added, while 10 mL of distilled water was taken and added to another small glass vial to add Nessler as a blank control sample. The concentration of NH₄⁺ was quantified by Nessler's reagent spectrophotometry (Nessler's reagent method) and ion chromatography (ICS-1100). The concentration–absorbance curve was calibrated using a standard ammonia solution with a series of concentrations (Figure S1). The fitting curve ($y = 0.1123x - 0.0027$, R² = 0.999) showed a good linear relation between absorbance value and ammonia concentration. Additionally, a standard curve of ammonia determined by ion chromatography is presented in Figure S2. The calibration curve ($y = 0.2286x - 0.0019$, R² = 0.999) was plotted based on peak area versus the concentration of ammonia. Then, apparent quantum efficiency (AQE) was further measured under filters of different wavelengths (300, 400, 500, and 600 nm). The photon flux of the incident light was measured with an optical power meter (CEL-NP2000-2(10)a, Beijing, China). AQE was calculated according to Equation (1) as follows:

$$\text{AQE} = \frac{N_e}{N_p} \times 100\% = \frac{3 \cdot n_{AM} \cdot N_A}{\frac{W \cdot A \cdot t}{h \cdot v}} \times 100\% \quad (1)$$

where N_e and N_p are the total number of reactive electrons transferred and the number of incident photons, respectively. n_{AM}, W, A, t, and v represent the molar number of generated ammonia (mol), the incident light intensity (measured as 491 mW cm⁻²), the irradiation area (cm²), the time (s), and the frequency, respectively. N_A and h are the Avogadro's constant (6.02×10^{23} /mol) and Planck constant ($6.62607015 \times 10^{-34}$ J·s), respectively.

2.5. Electrochemical Tests

The electrochemical measurements were taken on a CHI 660E electrochemical workstation. A standard three-electrode system consists of a working electrode, a graphite carbon rod as a counter electrode, and a saturated calomel electrode as a reference electrode. The working electrode was prepared by depositing tin fluoride oxide (FTO) on the sample membrane. Typically, 5 mg of photocatalyst and 20 μL of Nafion were dispersed in 200 μL of deionized water, then 40 μL of solution was immersed on 1 × 1 cm² FTO glass and then dried at room temperature. The transient photocurrent and the electrochemical impedance spectroscopy (EIS) of different samples were analyzed in a 0.5 M Na₂SO₄ aqueous solution.

3. Results and Discussion

3.1. Structural and Surface Characterizations

Figure 2 displays the SEM and TEM images of UiO-66 and Au/Uio-66. The SEM images of the as-prepared UiO-66 show that it was an ortho-octahedral structure with a particle size of around 200 nm (Figures 2a and S3). After modification, the obtained Au/Uio-66 had the same structure as UiO-66, but it had better dispersion (Figure 2b). Additionally, as shown in Figure 2c, black particles with isolated bright spots loaded onto UiO-66 were seen in the TEM image of Au/Uio-66, indicating a nanoscale-dispersed Au species. The nanoscale microstructure of Au was further characterized using a high-resolution trans-

mission electron microscope (HRTEM) (Figure 2d). In addition, EDX elemental mapping images of Au/UiO-66 were obtained (Figure 2e,f), and the results demonstrated that C, O, Zr, and Au achieved a uniform distribution over the entire skeleton of the scaffold. The results mentioned above confirmed that Au nanoparticles were uniformly dispersed on the surface of UiO-66.

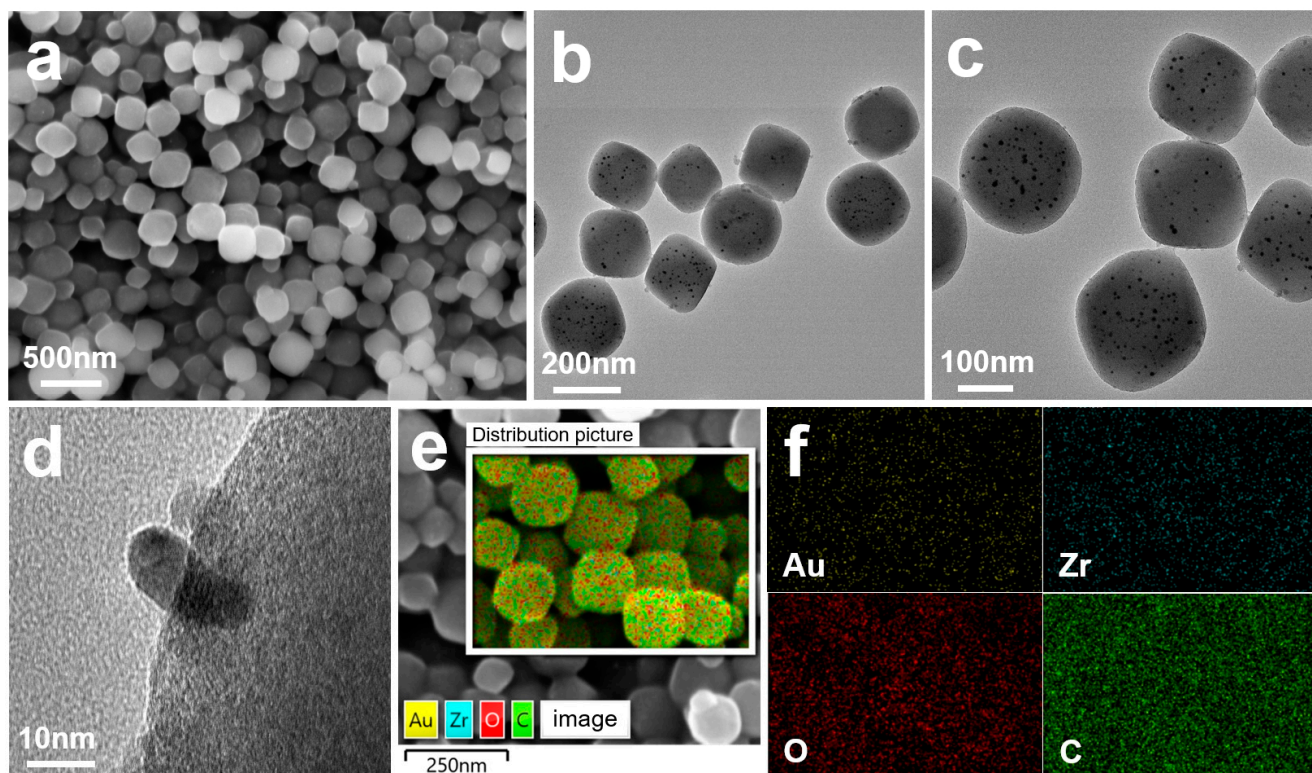


Figure 2. (a) SEM image of UiO-66; (b,c) TEM images of Au/UiO-66 at different magnifications; (d) HRTEM image of Au/UiO-66; and (e,f) EDX elemental mapping images of Au/UiO-66 with Au (yellow), Zr (blue), O (red), and C (green) distributions.

The XRD patterns of UiO-66 and the x wt% Au/UiO-66 ($x = 0.5, 1.0, 1.5, 2.0, 3.0$) samples are shown in Figure 3a. When Au was loaded onto UiO-66, the behavior of the main diffraction peaks was similar to that of UiO-66, and no diffraction peaks of the Au species were detected, which might be due to the fact that the content of loaded Au was low and the dispersion was high. In addition, the introduction of Au sites did not induce a phase transition in the UiO-66 crystals. As the Au content increased, the intensity of the characteristic peaks first increased and then decreased. This indicated that the Au nanoparticles had been successfully loaded onto UiO-66 [48].

X-ray photoelectron spectroscopy (XPS) was used to further probe the surface chemical state of the samples. As seen from the full spectrum of XPS, peaks of C, O, and Zr were observed in both samples (Figure S4). After the introduction of Au nanoparticles, the peaks of Au were not detected in Au/UiO-66, which might be explained by the low loading of Au. Figure 3b shows the Zr 3d spectra of the samples, and the peaks of Zr 3d_{5/2} and Zr 3d_{3/2} can be seen at 182.9 eV and 185.3 eV, corresponding to the Zr⁴⁺ oxidation state [49]. The O 1s spectra of the two samples were divided into three peaks at 530.3, 531.7, and 532.8 eV (Figure 3c), which belong to Zr-O, O-C/O-C, and -OH, respectively [50]. Compared with UiO-66, the Zr and O peaks of Au/UiO-66 moved to higher binding energies, implying that there were interactions between Au and UiO-66 carriers, accelerating electron transfer from UiO-66 to Au. Figure 3d shows the Au 4f spectrum of Au/UiO-66, with two peaks at 84.0 and 87.6 eV corresponding to Au⁰ and two peaks at 85.5 and 89.5 eV corresponding

to Au^+ [51]. This further proves that the Au nanoparticles have been successfully loaded onto UiO-66.

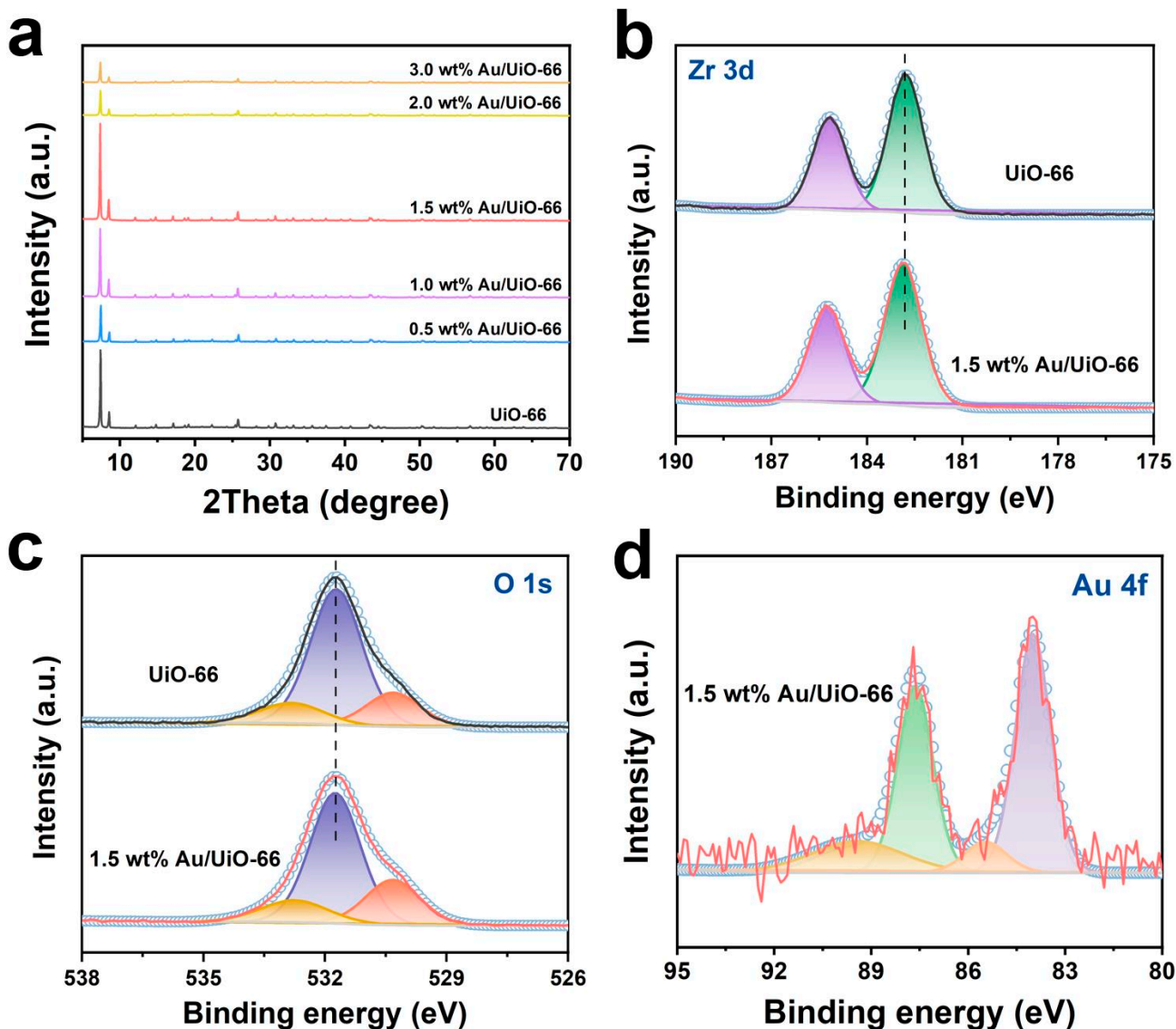


Figure 3. (a) XRD patterns of UiO-66 and x wt% Au/UiO-66 ($x = 0.5, 1.0, 1.5, 2.0, 3.0$); (b) XPS spectra for Zr 3d; (c) O 1s of UiO-66 and Au/UiO-66; and (d) XPS spectra for Au 4f of Au/UiO-66.

3.2. Photocatalyst Performance Analysis

The synthesized samples were tested for photocatalytic N_2 reduction under a 300 W xenon lamp, and the nitrogen fixation properties of the catalyst were assessed by detecting the ammonia yield (Figure 4). The ammonia concentration was measured using Nessler's reagent method and confirmed via the ion chromatography method. Figure 4a shows the activity plots for photocatalytic ammonia production of the x wt% Au/UiO-66 ($x = 0.5, 1.0, 1.5, 2.0, 3.0$) samples with different loadings. Pure UiO-66 had a low ammonia synthesis activity of $14.14 \mu\text{mol g}^{-1} \text{ h}^{-1}$. The ammonia production first improved and then declined with Au loading. The highest activity was observed at a loading of 1.5 wt%, reaching $66.28 \mu\text{mol g}^{-1} \text{ h}^{-1}$, which was about 4.7 times that of pure UiO-66. However, the ammonia generation rate gradually decreased when the loading exceeded 1.5%, which might be caused by the higher amount of Au saturating the surface active sites or the aggregation of Au [22,35]. Later on, the nitrogen fixation activity of M/UiO-66 (M = Pt, Pd, Au, Ag, Ru) with different metal loadings was tested (Figure 3d). The higher activity of metal-modified UiO-66 compared to pristine UiO-66 was in agreement with the literature reporting that

Au favored the nitrogen fixation reaction of UiO-66 [36,44]. Thus, Au preferred to create π orbital feedback to adsorb N_2 and used the excess empty orbitals to act as active centers to undermine the $N\equiv N$ bonding, which also proved that the choice of an adequate noble metal could promote the NRR reaction. The concentration of NH_4^+ was further determined using the ion chromatography method (Figure S5), and the two methods were almost identical in the detection of ammonia, which ensured the accuracy of Nessler's reagent method for determining NH_3 concentrations. Compared with other UiO-66-based photocatalysts, the Au/UiO-66 photocatalyst prepared in this work exhibited high photocatalytic activity, which was superior to previously reported photocatalysts (Table 1).

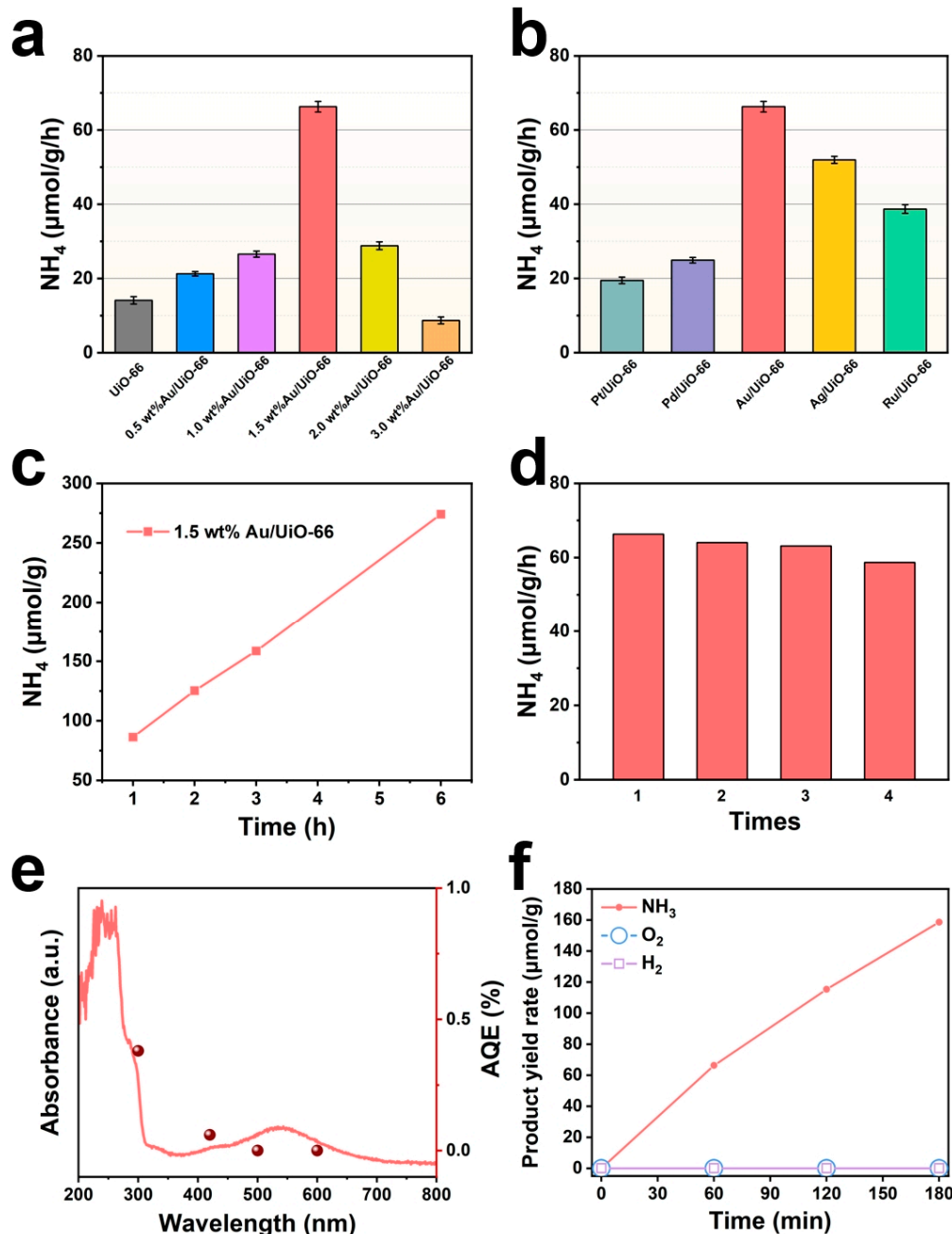


Figure 4. Photocatalytic N_2 fixation performances of UiO-66 with (a) different Au loading amounts, (b) different metal loadings (Pt, Pd, Au, Ag, Ru), (c) Au/UiO-66 photocatalytic ammonia production activity with time, (d) photocatalytic NH_3 production rate for cyclic tests of Au/UiO-66, (e) calculated AQEs (brown dots) for N_2 fixation over Au/UiO-66 along with its light absorption spectrum (red line), and (f) NH_3 , O_2 , and H_2 production rates of Au/UiO-66 under 300 W Xenon lamp irradiation.

Table 1. Summary of photocatalytic N₂ fixation on UiO-66-based catalysts in the recent literature.

Catalyst	Sacrificial Agent	Light Source	NH ₃ Yield (μmol gcat ⁻¹ h ⁻¹)	Ref.
UiO-66 (SH) ₂	No	300 W Xe lamp	32.38	[33]
Ru ₁ /d-UiO-66	No	300 W Xe lamp	53.28	[22]
UiO-66/PDA/CNNS	K ₂ SO ₃	Full spectrum	147.8	[52]
UiO-66-HAc	No	Full spectrum	31.81	[53]
MoS ₂ /UiO-66 (SH) ₂	No	Visible light (λ > 400 nm)	54.08	[54]
Au/UiO-66	No	Full spectrum	66.28	This work

Chemical stability was an important parameter for the evaluation of the catalyst. In addition, the stability of Au/UiO-66 was also examined through extended-duration experiments and cyclic tests (Figure 4c,d). The results indicated that Au/UiO-66 activity increased linearly within 6 h, and the ammonia yield reached 274.1 μmol/g at 6 h (Figure 4c). In the continuous photocatalytic nitrogen fixation test, the activity of Au/UiO-66 for ammonia synthesis had a negligible decrease after four cycles while maintaining high productivity (Figure 4d). This indicated that Au/UiO-66 had high chemical stability for photocatalytic nitrogen fixation.

In order to assess the efficiency of the use of light, the corresponding apparent quantum efficiency (AQE) was determined by testing different wavelengths of monochromatic light. As shown in Figure 4e, AQE decreased with increasing wavelengths of monochromatic light, with an AQE of 0.38% at 300 nm, 0.06% at 400 nm, and 0% at 500 nm and 600 nm, which was in good agreement with the DRS test of Au/UiO-66.

For the oxidation products (Figure 4f), no O₂ was detected in the photocatalytic products over Au/UiO-66 with increasing light illumination time. Moreover, a gradual increase in the detection of ammonia confirmed that the Au/UiO-66 photocatalyst contributed to N₂ fixation. Notably, no H₂ was detected during the photocatalytic process, which indicated the excellent selectivity of Au/UiO-66 for ammonia synthesis.

3.3. Optical and Electronic Properties

The synthesized samples were characterized using UV-vis DRS to probe the light absorption as well as the forbidden band width of the catalyst. As shown in Figure 5a, it was observed that UiO-66 had a very low visible light absorption, but after loading a trace amount of Au, the absorption band edges of x wt% Au/UiO-66 red-shifted, leading to a significant increase in the absorption of light. This could be explained by the fact that the loading of Au broadened the range of light absorption. Meanwhile, by converting the UV-vis DRS into the corresponding Tauc plot, according to the intercept of the tangent, the E_g values of UiO-66 and Au/UiO-66 were computed to be 4.05 and 3.94 eV, respectively (Figure 5b). Therefore, the light absorption and band gap results indicated that Au loading via the UV reduction method could effectively reduce the bandwidth of UiO-66. In addition, the valence band (VB) spectrum of XPS showed that the E_{VB} values of UiO-66 and Au/UiO-66 were estimated to be 3.13 and 2.97 eV, respectively, as determined by VB-XPS mapping (Figure 5c). According to the band gap equation (E_g = E_{VB} – E_{CB}) [1], the E_{CB} values of UiO-66 and Au/UiO-66 were calculated to be -0.92 and -0.97 eV, respectively. In addition, the slightly higher CB after Fe doping was thermodynamically more conducive to the photoreduction reaction of nitrogen. From this, the energy band schematics of UiO-66 and Au/UiO-66 could be established (Figure 5d). The results indicated that the reduced forbidden bandwidth of Au/UiO-66 enabled it to respond to incident light over a wider range and to be excited to produce more carriers, giving the material a greater potential for ammonia production.

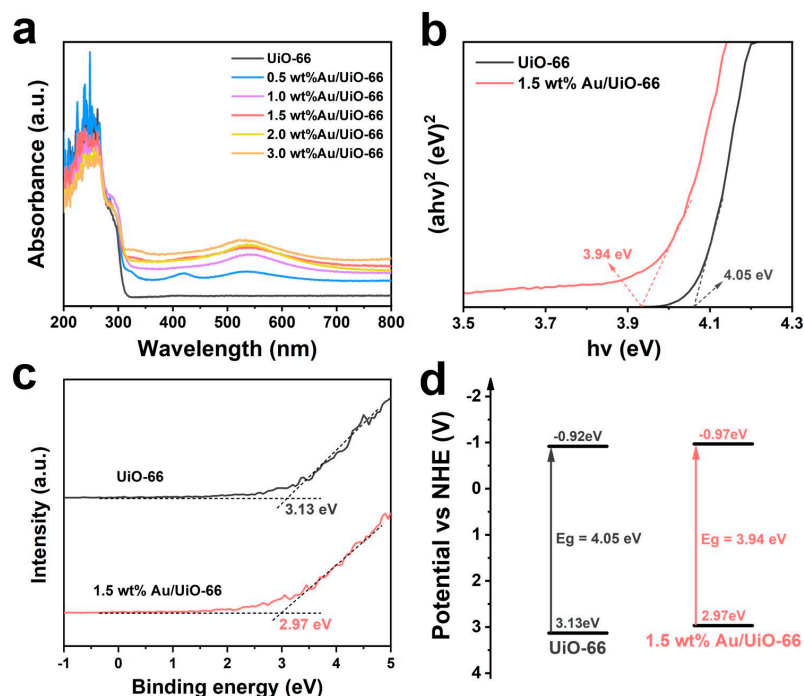


Figure 5. (a) DRS spectra, (b) Tauc plots, (c) XPS valence spectra, and (d) band structure of $\text{UiO}-66$ and $\text{Au}/\text{UiO}-66$.

Photoluminescence, hole separation, and carrier dynamics are important components of photocatalysis. In order to compare with $\text{UiO}-66$ and research the reason for the enhanced photocatalytic activity of $\text{Au}/\text{UiO}-66$, photoluminescence spectra (PL), photocurrent response, and electrochemical impedance spectroscopy (EIS) were further measured. The PL spectrum of $\text{Au}/\text{UiO}-66$ was tested under 550 nm laser excitation and is shown in Figure 6a. In general, the weaker the fluorescence intensity, the stronger the carrier separation ability [55]. It could be seen that both $\text{UiO}-66$ and $\text{Au}/\text{UiO}-66$ had strong emission peaks near 400 nm. Compared to $\text{UiO}-66$, the intensity of $\text{Au}/\text{UiO}-66$ was less pronounced, indicating a more effective inhibition of the complex reaction of the photogenerated electron–hole pair in $\text{Au}/\text{UiO}-66$ after the loading of Au nanoparticles. Therefore, it was likely that this was one of the factors that improved the efficiency of photocatalytic nitrogen fixation. Figure 6b shows the photocurrent response. $\text{UiO}-66$ had the lowest photocurrent response because of the quick complexation of photogenerated carriers on $\text{UiO}-66$. It can also be seen that the responsivity of $\text{Au}/\text{UiO}-66$ was much higher than that of $\text{UiO}-66$, which indicated that the loading of Au greatly suppressed the complexation of electron–hole pairs, allowing $\text{Au}/\text{UiO}-66$ to capture more visible photons. Subsequently, EIS tests were performed on the samples (Figure 6c), yielding results identical to those observed in the photocurrent. $\text{UiO}-66$ had large charge transfer resistance. With the photoreduction method to load Au, $\text{Au}/\text{UiO}-66$ has the smallest arc radius, indicating that its charge transfer resistance is smaller, which favors the separation of electrons and holes. The above results indicated that $\text{Au}/\text{UiO}-66$ had a stronger charge transfer capability and a lower carrier recombination rate, which was more favorable for the separation and migration of electrons and holes, allowing higher charge transfer efficiency and a lower possibility of charge recombination, thereby enhancing the utilization of photogenerated electrons.

According to the above experimental results, a probable reaction mechanism for photocatalytic N_2 fixation by $\text{Au}/\text{UiO}-66$ was proposed, as shown in Figure 7. N_2 was easily adsorbed by $\text{UiO}-66$'s pores [33,54], and the redox reaction took place inside the catalyst, which lowered the transfer distance of electrons and facilitated the subsequent reaction. As shown in Figure 7, under light irradiation, $\text{Au}/\text{UiO}-66$ was excited to produce electrons and holes in CB and VB. The ligand H_2BDC in $\text{Au}/\text{UiO}-66$ was excited under light

irradiation, and electrons were transported from the excited ligand to the Au nanoparticles. The Au nanoparticles transferred the obtained electrons to N_2 to make it react in a reduction reaction to lose electrons, and they reacted with the hydrogen atoms to produce ammonia gas. Moreover, the Au nanoparticles continuously received the electrons generated by the ligand, which eventually led to the synthesis of ammonia [33]. Therefore, Au/UiO-66 had a strong photocatalytic nitrogen fixation performance under environmental conditions.

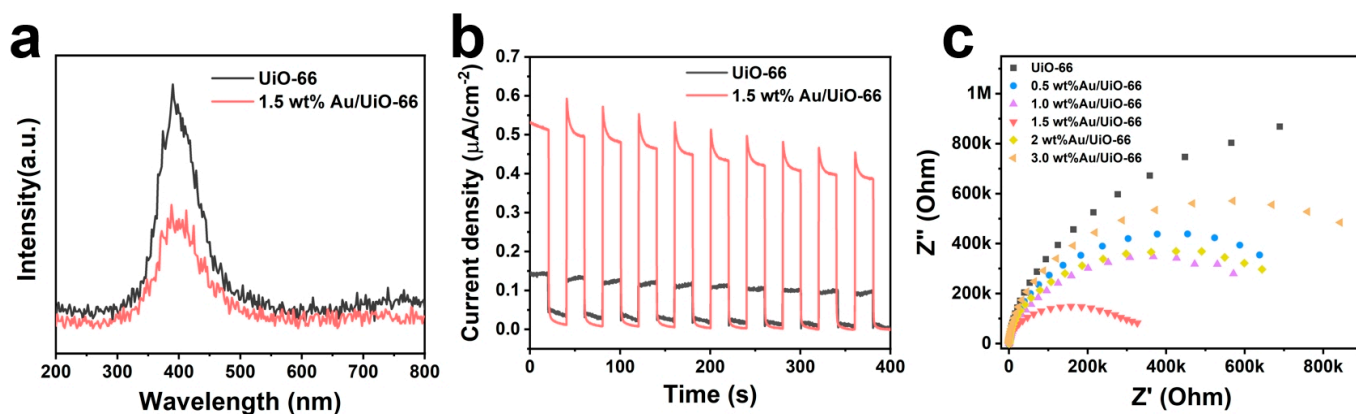


Figure 6. (a) PL spectra, (b) photocurrent response, and (c) EIS spectra of UiO-66 and Au/UiO-66.

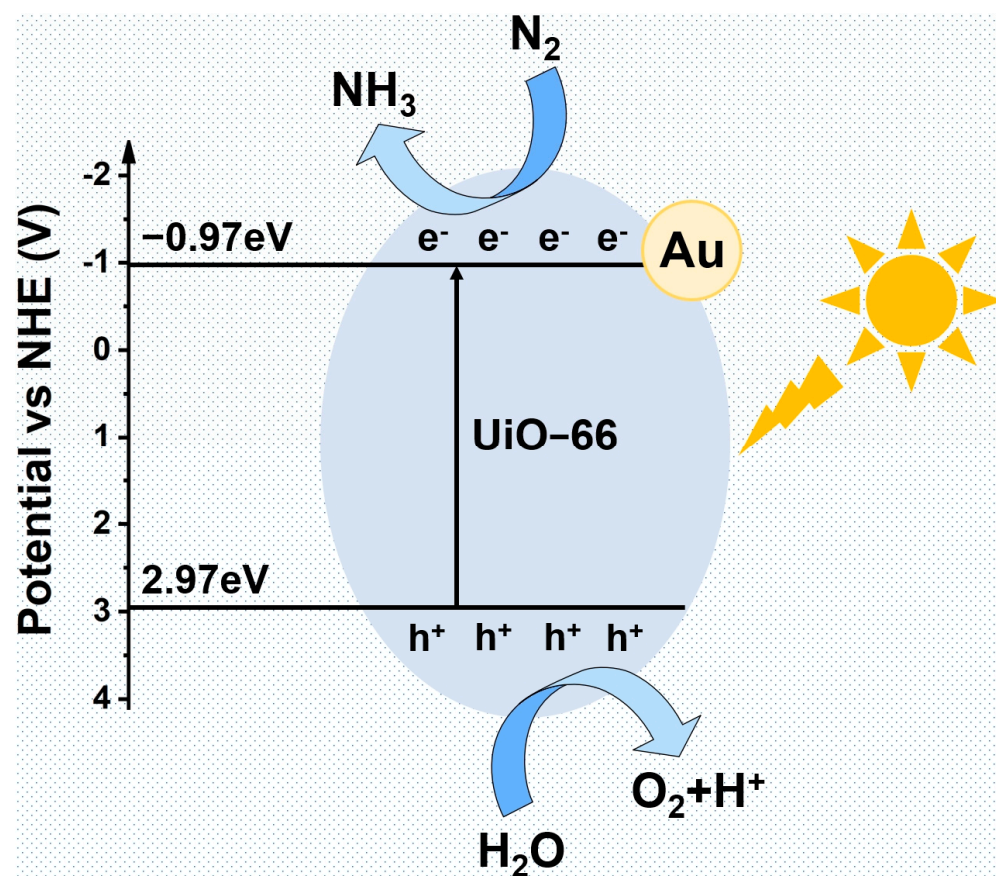


Figure 7. Possible mechanism of photocatalytic N_2 fixation by Au/UiO-66 under simulated solar light irradiation.

4. Conclusions

In summary, we synthesized Au/UiO-66 with a photocatalytic N_2 reduction function by inducing UiO-66 with UV light. The experimental results indicated that the synthesized Au/UiO-66 photocatalysts produced an ammonia yield of $66.28 \mu\text{mol g}^{-1} \text{ h}^{-1}$ without

using a sacrificial agent. This yield was 4.7 times higher than that of pure UiO-66 and maintained good stability within 6 h. It was shown that the nanoscale-dispersed Au was stably loaded onto UiO-66, which provided an electron-rich environment for NRR. The present work not only provided an attractive MOF-based material for photocatalytic nitrogen fixation but also a new idea to further research the synergistic interaction between nanoparticles and MOFs to improve the performance of artificial N₂ immobilization.

Supplementary Materials: The following supporting information can be downloaded at: <https://www.mdpi.com/article/10.3390/pr12010064/s1>, Figure S1: (a) Standard curves for NH₄⁺ with Nessler's reagent and (b) chromogenic reaction of Nessler's reagent with NH₄⁺ ions; Figure S2: Calibration curve used for calculation of NH₄⁺ concentrations using ion chromatogram method; Figure S3: SEM image of UiO-66; Figure S4: XPS survey spectra of UiO-66 and Au/UiO-66 samples; Figure S5: Ion chromatography profile.

Author Contributions: Conceptualization, X.M. and Z.L.; methodology, G.R. and Z.Z.; software, G.R.; validation, Z.Z.; formal analysis, G.R.; investigation, G.R. and Z.Z.; resources, X.M.; data curation, Z.Z. and G.R.; writing—original draft preparation, Z.Z.; writing—review and editing, X.M.; visualization, Z.L.; supervision, X.M.; project administration, X.M.; funding acquisition, X.M. All authors have read and agreed to the published version of the manuscript.

Funding: This work was financially supported by the National Natural Science Foundation of China (Grant No. 22002146), the Shandong Provincial Natural Science Foundation (Grant No. ZR2021QB056), and the Fundamental Research Funds for the Central Universities (Grant No. 202261014).

Data Availability Statement: Data will be made available upon request from the corresponding author. The data are not publicly available due to privacy.

Acknowledgments: This work was financially supported by the National Natural Science Foundation of China (Grant No. 22002146), the Shandong Provincial Natural Science Foundation (Grant No. ZR2021QB056), and the Fundamental Research Funds for the Central Universities (Grant No. 202261014). The authors would like to thank the e-Testing Service Platform (<https://www.eceshi.com> (accessed on 6 January 2023)) for their assistance with the XRD, XPS, PL, and other analyses.

Conflicts of Interest: The authors declare no conflicts of interest.

References

1. Ren, G.; Shi, M.; Li, Z.; Zhang, Z.; Meng, X. Electronic metal-support interaction via defective-induced platinum modified BiOBr for photocatalytic N₂ fixation. *Appl. Catal. B Environ.* **2023**, *327*, 122462. [[CrossRef](#)]
2. MacFarlane, D.R.; Cherepanov, P.V.; Choi, J.; Suryanto, B.H.R.; Hodgetts, R.Y.; Bakker, J.M.; Vallana, F.M.F.; Simonov, A.N. A Roadmap to the Ammonia Economy. *Joule* **2020**, *4*, 1186–1205. [[CrossRef](#)]
3. Cui, X.; Tang, C.; Zhang, Q. A Review of Electrocatalytic Reduction of Dinitrogen to Ammonia under Ambient Conditions. *Adv. Energy Mater.* **2018**, *8*, 1800369. [[CrossRef](#)]
4. Ren, G.; Liu, S.; Shi, M.; Zhang, Z.; Li, Z.; Meng, X. Ultraviolet Light-Modulated Defects on BiOBr to Improve the Photocatalytic Fixation of Nitrogen to Ammonia. *Sol. RRL* **2022**, *6*, 2200653. [[CrossRef](#)]
5. Zhang, G.; Sewell, C.D.; Zhang, P.; Mi, H.; Lin, Z. Nanostructured photocatalysts for nitrogen fixation. *Nano Energy* **2020**, *71*, 104645. [[CrossRef](#)]
6. Cheng, M.; Xiao, C.; Xie, Y. Photocatalytic nitrogen fixation: The role of defects in photocatalysts. *J. Mater. Chem. A* **2019**, *7*, 19616–19633. [[CrossRef](#)]
7. Ren, G.; Shi, M.; Liu, S.; Li, Z.; Zhang, Z.; Meng, X. Molecular-level insight into photocatalytic reduction of N₂ over Ruthenium single atom modified TiO₂ by electronic Metal-support interaction. *Chem. Eng. J.* **2023**, *454*, 140158. [[CrossRef](#)]
8. Shi, R.; Zhang, X.; Waterhouse, G.I.N.; Zhao, Y.; Zhang, T. The Journey toward Low Temperature, Low Pressure Catalytic Nitrogen Fixation. *Adv. Energy Mater.* **2020**, *10*, 2000659. [[CrossRef](#)]
9. Yin, H.; Chen, Z.; Peng, Y.; Xiong, S.; Li, Y.; Yamashita, H.; Li, J. Dual Active Centers Bridged by Oxygen Vacancies of Ruthenium Single-Atom Hybrids Supported on Molybdenum Oxide for Photocatalytic Ammonia Synthesis. *Angew. Chem. Int. Ed.* **2022**, *61*, e202114242. [[CrossRef](#)]
10. Zhao, Y.; Zhao, Y.; Waterhouse, G.I.N.; Zheng, L.; Cao, X.; Teng, F.; Wu, L.Z.; Tung, C.H.; O'Hare, D.; Zhang, T. Layered-Double-Hydroxide Nanosheets as Efficient Visible-Light-Driven Photocatalysts for Dinitrogen Fixation. *Adv. Mater.* **2017**, *29*, 1703828. [[CrossRef](#)]

11. Hrndi, J.; Xia, J.; Chisholm, M.F.; Zhong, J.; Chen, C.; Cao, X.; Dong, F.; Chi, Z.; Chen, H.; Weng, Y.X.; et al. Defect-Tailoring Mediated Electron-Hole Separation in Single-Unit-Cell $\text{Bi}_3\text{O}_4\text{Br}$ Nanosheets for Boosting Photocatalytic Hydrogen Evolution and Nitrogen Fixation. *Adv. Mater.* **2019**, *31*, e1807576.
12. Li, P.; Zhou, Z.; Wang, Q.; Guo, M.; Chen, S.; Low, J.; Long, R.; Liu, W.; Ding, P.; Wu, Y.; et al. Visible-Light-Driven Nitrogen Fixation Catalyzed by $\text{Bi}_5\text{O}_7\text{Br}$ Nanostructures: Enhanced Performance by Oxygen Vacancies. *J. Am. Chem. Soc.* **2020**, *142*, 12430–12439. [[CrossRef](#)] [[PubMed](#)]
13. Liu, H.; Cheng, M.; Liu, Y.; Wang, J.; Zhang, G.; Li, L.; Du, L.; Wang, G.; Yang, S.; Wang, X.J.E. Science, Single atoms meet metal–organic frameworks: Collaborative efforts for efficient photocatalysis. *Energy Environ. Sci.* **2022**, *15*, 3722–3749. [[CrossRef](#)]
14. Gao, D.; Xu, J.; Wang, L.; Zhu, B.; Yu, H.; Yu, J.J.A.M. Optimizing atomic hydrogen desorption of sulfur-rich NiS_{1+x} cocatalyst for boosting photocatalytic H_2 evolution. *Adv. Mater.* **2022**, *34*, 2108475. [[CrossRef](#)] [[PubMed](#)]
15. Yang, C.; Zhang, Y.; Yue, F.; Du, R.; Ma, T.; Bian, Y.; Li, R.; Guo, L.; Wang, D.; Fu, F.J.A.C.B.E. Co doping regulating electronic structure of Bi_2MoO_6 to construct dual active sites for photocatalytic nitrogen fixation. *Appl. Catal. B Environ.* **2023**, *338*, 123057. [[CrossRef](#)]
16. Forrest, S.J.; Schluschaß, B.; Yuzik-Klimova, E.Y.; Schneider, S.J.C.R. Nitrogen fixation via splitting into nitrido complexes. *Chem. Rev.* **2021**, *121*, 6522–6587. [[CrossRef](#)] [[PubMed](#)]
17. Clark, C.A.; Heck, K.N.; Powell, C.D.; Wong, M.S. Highly Defective UiO-66 Materials for the Adsorptive Removal of Perfluoroctanesulfonate. *ACS Sustain. Chem. Eng.* **2019**, *7*, 6619–6628. [[CrossRef](#)]
18. Qiu, T.; Liang, Z.; Guo, W.; Tabassum, H.; Gao, S.; Zou, R. Metal-Organic Framework-Based Materials for Energy Conversion and Storage. *ACS Energy Lett.* **2020**, *5*, 520–532. [[CrossRef](#)]
19. Yuan, S.; Zhang, J.; Hu, L.; Li, J.; Li, S.; Gao, Y.; Zhang, Q.; Gu, L.; Yang, W.; Feng, X.; et al. Decarboxylation-Induced Defects in MOF-Derived Single Cobalt Atom@Carbon Electrocatalysts for Efficient Oxygen Reduction. *Angew. Chem. Int. Ed.* **2021**, *60*, 21685–21690. [[CrossRef](#)]
20. Wang, G.; He, C.-T.; Huang, R.; Mao, J.; Wang, D.; Li, Y. Photoinduction of Cu Single Atoms Decorated on UiO-66-NH₂ for Enhanced Photocatalytic Reduction of CO₂ to Liquid Fuels. *J. Am. Chem. Soc.* **2020**, *142*, 19339–19345. [[CrossRef](#)]
21. Xu, C.; Pan, Y.; Wan, G.; Liu, H.; Wang, L.; Zhou, H.; Yu, S.-H.; Jiang, H.-L. Turning on Visible-Light Photocatalytic C-H Oxidation over Metal-Organic Frameworks by Introducing Metal-to-Cluster Charge Transfer. *J. Am. Chem. Soc.* **2019**, *141*, 19110–19117. [[CrossRef](#)] [[PubMed](#)]
22. Ren, G.; Zhao, J.; Zhao, Z.; Li, Z.; Wang, L.; Zhang, Z.; Li, C.; Meng, X. Defects-Induced Single-Atom Anchoring on Metal-Organic Frameworks for High-Efficiency Photocatalytic Nitrogen Reduction. *Angew. Chem. Int. Ed. Engl.* **2023**, *e202314408*. [[CrossRef](#)]
23. Crake, A.; Christoforidis, K.C.; Gregg, A.; Moss, B.; Kafizas, A.; Petit, C. The Effect of Materials Architecture in TiO₂/MOF Composites on CO₂ Photoreduction and Charge Transfer. *Small* **2019**, *15*, e1805473. [[CrossRef](#)] [[PubMed](#)]
24. Yuan, Y.-P.; Yin, L.-S.; Cao, S.-W.; Xu, G.-S.; Li, C.-H.; Xue, C. Improving photocatalytic hydrogen production of metal-organic framework UiO-66 octahedrons by dye-sensitization. *Appl. Catal. B Environ.* **2015**, *168–169*, 572–576. [[CrossRef](#)]
25. Benseghir, Y.; Lemarchand, A.; Duguet, M.; Mialane, P.; Gomez-Mingot, M.; Roch-Marchal, C.; Pino, T.; Ha-Thi, M.H.; Haouas, M.; Fontecave, M.; et al. Co-immobilization of a Rh Catalyst and a Keggin Polyoxometalate in the UiO-67 Zr-Based Metal-Organic Framework: In Depth Structural Characterization and Photocatalytic Properties for CO₂ Reduction. *J. Am. Chem. Soc.* **2020**, *142*, 9428–9438. [[CrossRef](#)] [[PubMed](#)]
26. Kratzl, K.; Kratky, T.; Gunther, S.; Tomanec, O.; Zboril, R.; Michalicka, J.; Macak, J.M.; Cokoja, M.; Fischer, R.A. Generation and Stabilization of Small Platinum Clusters Pt_(12+/-x) Inside a Metal-Organic Framework. *J. Am. Chem. Soc.* **2019**, *141*, 13962–13969. [[CrossRef](#)]
27. Jiao, L.; Wang, Y.; Jiang, H.L.; Xu, Q. Metal-Organic Frameworks as Platforms for Catalytic Applications. *Adv. Mater.* **2018**, *30*, e1703663. [[CrossRef](#)] [[PubMed](#)]
28. Mo, Q.; Zhang, L.; Li, S.; Song, H.; Fan, Y.; Su, C.Y. Engineering Single-Atom Sites into Pore-Confining Nanospaces of Porphyrinic Metal-Organic Frameworks for the Highly Efficient Photocatalytic Hydrogen Evolution Reaction. *J. Am. Chem. Soc.* **2022**, *144*, 22747–22758. [[CrossRef](#)]
29. Ma, Y.; Han, X.; Xu, S.; Wang, Z.; Li, W.; da Silva, I.; Chansai, S.; Lee, D.; Zou, Y.; Nikiel, M.; et al. Atomically Dispersed Copper Sites in a Metal-Organic Framework for Reduction of Nitrogen Dioxide. *J. Am. Chem. Soc.* **2021**, *143*, 10977–10985. [[CrossRef](#)]
30. Zhu, Y.; Zheng, J.; Ye, J.; Cui, Y.; Koh, K.; Kovarik, L.; Camaioni, D.M.; Fulton, J.L.; Truhlar, D.G.; Neurock, M.; et al. Copper-zirconia interfaces in UiO-66 enable selective catalytic hydrogenation of CO₂ to methanol. *Nat. Commun.* **2020**, *11*, 5849. [[CrossRef](#)]
31. Yang, T.; Zhang, L.; Zhong, L.; Han, X.; Dong, S.; Li, Y. Selective adsorption of Ag(I) ions with poly (vinyl alcohol) modified with thiourea (TU-PVA). *Hydrometallurgy* **2018**, *175*, 179–186. [[CrossRef](#)]
32. Hu, K.; Huang, Z.; Zeng, L.; Zhang, Z.; Mei, L.; Chai, Z.; Shi, W. Recent Advances in MOF-Based Materials for Photocatalytic Nitrogen Fixation. *Eur. J. Inorg. Chem.* **2022**, *2022*, e202100748. [[CrossRef](#)]
33. Guo, B.; Cheng, X.; Tang, Y.; Guo, W.; Deng, S.; Wu, L.; Fu, X. Dehydrated UiO-66(SH)₂: The Zr-O Cluster and Its Photocatalytic Role Mimicking the Biological Nitrogen Fixation. *Angew. Chem. Int. Ed.* **2022**, *61*, e202117244. [[CrossRef](#)] [[PubMed](#)]
34. Dong, C.; Wei, F.; Li, J.; Lu, Q.; Han, X. Uniform octahedral ZrO₂@C from carbonized UiO-66 for electrocatalytic nitrogen reduction. *Mater. Today Energy* **2021**, *22*, 100884. [[CrossRef](#)]

35. Gao, W.; Li, X.; Zhang, X.; Su, S.; Luo, S.; Huang, R.; Jing, Y.; Luo, M. Photocatalytic nitrogen fixation of metal-organic frameworks (MOFs) excited by ultraviolet light: Insights into the nitrogen fixation mechanism of missing metal cluster or linker defects. *Nanoscale* **2021**, *13*, 7801–7809. [CrossRef] [PubMed]
36. Leus, K.; Concepcion, P.; Vandichel, M.; Meledina, M.; Grirrane, A.; Esquivel, D.; Turner, S.; Poelman, D.; Waroquier, M.; Van Speybroeck, V.; et al. Au@UiO-66: A base free oxidation catalyst. *RSC Adv.* **2015**, *5*, 22334–22342. [CrossRef]
37. Zhang, W.; Shi, W.; Ji, W.; Wu, H.; Gu, Z.; Wang, P.; Li, X.; Qin, P.; Zhang, J.; Fan, Y.; et al. Microenvironment of MOF Channel Coordination with Pt NPs for Selective Hydrogenation of Unsaturated Aldehydes. *ACS Catal.* **2020**, *10*, 5805–5813. [CrossRef]
38. Bai, X.; Ma, W.; Liu, P.; Sun, Q.; Zhang, K.; Li, A.; Pan, J.; Lyu, Z. Catalytic TFN membranes containing MOF loaded Ag NPs prepared by interfacial polymerization. *Microporous Mesoporous Mater.* **2022**, *335*, 111811. [CrossRef]
39. Sadeghi, S.; Jafarzadeh, M.; Abbasi, A.R.; Daasbjerg, K. Incorporation of CuO NPs into modified UiO-66-NH₂ metal-organic frameworks (MOFs) with melamine for catalytic C–O coupling in the Ullmann condensation. *New J. Chem.* **2017**, *41*, 12014–12027. [CrossRef]
40. Zhang, X.; Li, X.; Su, S.; Tan, M.; Liu, G.; Wang, Y.; Luo, M. Ag nanoparticles in the cages of MIL-101(Cr) as an efficient and stable photocatalyst for nitrogen reduction reaction. *Catal. Sci. Technol.* **2023**, *13*, 705–713. [CrossRef]
41. Yan, S.; Zhang, X.; Wu, D.; Yu, Y.; Ding, Z. A system investigation on Ru-MOF-74 with efficient photocatalytic nitrogen fixation performance. *Surf. Interfaces* **2022**, *33*, 102225. [CrossRef]
42. Zhang, J.; Bai, T.; Huang, H.; Yu, M.H.; Fan, X.; Chang, Z.; Bu, X.H. Metal-Organic-Framework-Based Photocatalysts Optimized by Spatially Separated Cocatalysts for Overall Water Splitting. *Adv. Mater.* **2020**, *32*, e2004747. [CrossRef] [PubMed]
43. Nazemi, M.; El-Sayed, M.A. Plasmon-enhanced photo(electro)chemical nitrogen fixation under ambient conditions using visible light responsive hybrid hollow Au-Ag₂O nanocages. *Nano Energy* **2019**, *63*, 103886. [CrossRef]
44. Yu, X.; Qiu, H.; Wang, Z.; Wang, B.; Meng, Q.; Sun, S.; Tang, Y.; Zhao, K. Constructing the Z-scheme TiO₂/Au/BiOI nanocomposite for enhanced photocatalytic nitrogen fixation. *Appl. Surf. Sci.* **2021**, *556*, 149785. [CrossRef]
45. Yao, X.; Wang, H.; Ma, Z.; Liu, M.; Zhao, X.; Jia, D. Adsorption of Hg(II) from aqueous solution using thiourea functionalized chelating fiber. *Chin. J. Chem. Eng.* **2016**, *24*, 1344–1352. [CrossRef]
46. Chen, L.W.; Hao, Y.C.; Guo, Y.; Zhang, Q.; Li, J.; Gao, W.Y.; Ren, L.; Su, X.; Hu, L.; Zhang, N.; et al. Metal-Organic Framework Membranes Encapsulating Gold Nanoparticles for Direct Plasmonic Photocatalytic Nitrogen Fixation. *J. Am. Chem. Soc.* **2021**, *143*, 5727–5736. [CrossRef]
47. Dolgopolova, E.A.; Rice, A.M.; Martin, C.R.; Shustova, N.B. Photochemistry and photophysics of MOFs: Steps towards MOF-based sensing enhancements. *Chem. Soc. Rev.* **2018**, *47*, 4710–4728. [CrossRef]
48. Xie, H.; Wan, Y.; Chen, H.; Xiong, G.; Wang, L.; Xu, Q.; Li, X.; Zhou, Q. Cr(VI) Adsorption from Aqueous Solution by UiO-66 Modified Corncob. *Sustainability* **2021**, *13*, 12962. [CrossRef]
49. Su, Y.; Zhang, Z.; Liu, H.; Wang, Y. Cd_{0.2}Zn_{0.8}S@UiO-66-NH₂ nanocomposites as efficient and stable visible-light-driven photocatalyst for H₂ evolution and CO₂ reduction. *Appl. Catal. B Environ.* **2017**, *200*, 448–457. [CrossRef]
50. Zhou, Z.; Chen, D.; Li, N.; Xu, Q.; Li, H.; He, J.; Lu, J. Three-Dimensional g-C₃N₄/NH₂-UiO-66 graphitic aerogel hybrids with recyclable property for enhanced photocatalytic elimination of nitric oxide. *Chem. Eng. J.* **2021**, *418*, 129117. [CrossRef]
51. El-Sayed, N.; Trouillet, V.; Clasen, A.; Jung, G.; Hollemeyer, K.; Schneider, M. NIR-Emitting Gold Nanoclusters-Modified Gelatin Nanoparticles as a Bioimaging Agent in Tissue. *Adv. Healthc. Mater.* **2019**, *8*, e1900993. [CrossRef] [PubMed]
52. Ren, H.; Tan, J.; Zhao, Z.; Shi, Y.; Xin, X.; Yang, D.; Jiang, Z. Multi-stepwise electron transfer via MOF-based nanocomposites for photocatalytic ammonia synthesis. *Catal. Sci. Technol.* **2022**, *12*, 5540–5548. [CrossRef]
53. He, X.; Liao, Y.; Tan, J.; Li, G.; Yin, F. Defective UiO-66 toward boosted electrochemical nitrogen reduction to ammonia. *Electrochim. Acta* **2022**, *409*, 139988. [CrossRef]
54. Li, Q.; Shi, Y.; Wang, Z.; Liu, C.; Bi, J.; Yu, J.C.; Wu, L. Nitrogen activation and surface charge regulation for enhancing the visible-light-driven N₂ fixation over MoS₂/UiO-66(SH)₂. *J. Colloid. Interface Sci.* **2023**, *652*, 1568–1577. [CrossRef]
55. Ren, G.; Liu, S.; Li, Z.; Bai, H.; Hu, X.; Meng, X. Highly Selective Photocatalytic Reduction of CO₂ to CO Over Ru-Modified Bi₂MoO₆. *Sol. RRL* **2022**, *6*, 2200154. [CrossRef]

Disclaimer/Publisher’s Note: The statements, opinions and data contained in all publications are solely those of the individual author(s) and contributor(s) and not of MDPI and/or the editor(s). MDPI and/or the editor(s) disclaim responsibility for any injury to people or property resulting from any ideas, methods, instructions or products referred to in the content.